PHYSICAL REVIEW B **90**, 214525 (2014)

Manipulating textures of rotating superfluid ^{3}He-A phase in a single narrow cylinder

T. Kunimatsu,[1,2,*] H. Nema,[1,3] R. Ishiguro,[4] M. Kubota,[2,5] T. Takagi,[6] Y. Sasaki,[7] and O. Ishikawa[1]

[1]*Graduate School of Science, Osaka City University, Osaka 558-8585, Japan*
[2]*Institute of Solid State Physics, University of Tokyo, Chiba 277-8581, Japan*
[3]*Faculty of Science and Engineering, Chuo University, Tokyo 112-8551, Japan*
[4]*Center for Emergent Matter Science, RIKEN, Saitama 351-0198, Japan*
[5]*Shibaura Institute of Technology, Tokyo 108-8548, Japan*
[6]*Department of Applied Physics, University of Fukui, Fukui 910-8507, Japan*
[7]*Research Center for Low Temperature and Materials Sciences, Kyoto University, Kyoto 606-8501, Japan*

(Received 7 July 2014; published 29 December 2014)

We investigated order parameter textures of the rotating superfluid ^{3}He-A phase in a single narrow cylinder with a diameter of about 10 times the dipole coherence length by the cw-NMR method. It is theoretically proposed that in such a narrow cylinder, a few special textures will appear due to the confinement in a cylindrical geometry. We observed three types of NMR spectra in the A phase. The NMR spectra of the textures were identified by a comparison with the spin waves excited in the NMR potential using their numerically calculated resonance frequencies and relative intensities. We have established a method to selectively generate each one of the textures by controlling the conditions when the A phase was formed, such as the applied magnetic field, rotation angular velocity, and temperature.

DOI: 10.1103/PhysRevB.90.214525 PACS number(s): 67.30.he, 67.30.er

Superfluid ^{3}He is well known as a BCS-type condensate with orbital p-wave ($L = 1$) and spin-triplet ($S = 1$) symmetry [1]. Rich degrees of freedom due to this order parameter symmetry give rise to characteristic properties of superfluid ^{3}He. A symmetry-breaking phase transition causes a formation of various topological defects such as vortices, domain walls, or textures. They play essential roles in various fields of physics, ranging from condensed matter physics [2] to particle physics [3] and cosmology [4]. We focuses on the texture, which is the spatial distribution of the order parameter. In the superfluid ^{3}He-A phase, the textures are described by the orbital component **l**-vectors and the spin component **d**-vectors. A boundary condition plays an important role to control the textures because the **l**-vectors are orientated perpendicular to the surface of the container. In the bulk A phase, the **l**- and **d**-vectors are parallel to each other to minimize the dipole energy, the so-called "dipole-locked state." However, characteristic textures are formed in restricted geometries [5–8].

We have investigated the texture in a narrow single cylinder with a diameter about ten times larger than the dipole coherence length, $\xi_D \approx 10$ μm. Earlier works [7,9] have shown that in this geometry, the vortex penetration does not occur within an available rotation and we can investigate only textures under our experimental condition. Some candidate textures formed in this geometry have been suggested for **l**- and **d**-vectors. For **l**-vectors, three types of textures have been proposed, the radial-disgyration (RD) texture [10] with one singularity at the center axis of the cylinder, the pan-am (PA) texture [11] with two singularities at the edge of opposite sides of the perimeter, and the Mermin-Ho (MH) texture [12] with no singularity. For **d**-vectors [13], the hyperbolic (hb) and axial (ax) textures have been proposed, whose space distributions are similar to those of the PA and MH textures, respectively. The radial-disgyration (rd) texture for **d**-vectors cannot be formed because singularities lead to large losses of condensation energy. Therefore there are six types of candidate textures from the combination of **l**- and **d**-vectors.

A crucial feature of the MH texture is that it possesses a spontaneous macroscopic circulating mass current without any external rotation. The RD texture may also possess the macroscopic circulating mass current under rotation. But the PA texture does not possess it. It is important that the texture formed in a narrow cylinder depends on not only the applied magnetic field and temperature but also the rotation angular velocity Ω around the cylinder axis because the free energy at a rotating frame $F_{\rm rot}$ is described as $F_{\rm rot} = F_{\rm rest} - \Omega L$, where $F_{\rm rest}$ is the free energy at rest and L is the angular momentum around the cylinder axis. The angular momentum of the A phase has attracted much interest because, in addition to an angular momentum which originates from the superflow, a contribution from the relative orbital angular momentum of the Cooper pair may exist. This has been a controversy over "the paradox of the orbital angular momentum" [14–16]. To further investigate the problem, one should establish a method to generate texture which might hold a macroscopic orbital angular momentum in the region of aligned **l**-texture.

NMR is a powerful tool for identifying textures. In particular, spin wave excitations in the A phase confined in a narrow cylinder are distinctive features and can be used as signatures of the texture. R_t^2 is a characteristic coefficient related to the resonance frequency of spin wave f, which is described by the frequency shift Δf from the Larmor frequency f_L as

$$\Delta f = f - f_L = R_t^2 \frac{f_A^2}{2 f_L}, \tag{1}$$

where f_A is the Leggett frequency of the A phase. The NMR spectra are analyzed by a comparison with numerically calculated spin waves using their resonance frequencies and

*kunimats@sci.osaka-cu.ac.jp

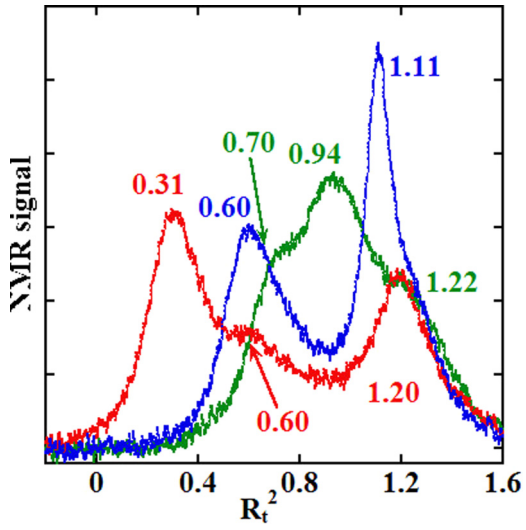

FIG. 1. (Color online) Typical cw-NMR spectra of three types of textures. Measurements were performed at $T = 0.80T_C$ and $\Omega = 0$ rad/s. Each spectrum was formed by a different process to enter the A phase. The numbers in the graph give R_t^2 of the NMR peaks.

relative intensities excited in the NMR potential formed by each texture [17], which is derived using Cross's expression of the free energy [18]. In the calculations, only ξ_D is considered a temperature-independent parameter to be adjusted because it is not known accurately.

We have studied the textures of the rotating A phase confined in narrow cylinders using the cw-NMR method and the rotating cryostat at ISSP [19]. In earlier works with a 150-cylinder bundled cell [20], three types of spin wave spectra, which depended on the process to form the A phase, were observed. However, it was hard to identify the textures because of the possibility that a different texture was formed with respect to each cylinder. We thus prepared a sample cell with a single narrow cylinder and have performed cw-NMR measurements. In this paper, we show the formation of the textures of the A phase confined in a single narrow cylinder and the nature of the spin waves excited in the formed textures.

Our cylinder cell [21] consists of a single polyimide tube with a radius R of 50 μm and a length of 15 mm. An NMR pickup coil is wound at the middle of the cylinder tube. The total amount of liquid inside the coil is only 40 nl. This sample cell was set in a rotating cryostat with the maximum rotating angular velocity set to $|\Omega| = 8$ rad/s. The pressure of the sample was set at 3.3 MPa. cw-NMR measurements were performed at 700 kHz (the corresponding static magnetic field was $H = 21.6$ mT). The static magnetic field and the rotational axis were parallel to the cylinder axis. The temperature was measured with a Pt NMR thermometer in the sample cell and by a melting curve thermometer (MCT) on the demagnetization stage.

With a single narrow cylinder, we observed three types of NMR spectra [21]. The typical three NMR spectra at $T = 0.80T_C$ and $\Omega = 0$ rad/s are shown in Fig. 1. The numbers written in the graph give R_t^2 of the peaks obtained using Eq. (1). R_t^2 of 0.31 in the red signal, 0.60 in the blue signal, and 0.94 in the green signal correspond to, respectively, 0.34, 0.59, and 0.84 at $T = 0.83T_C$ in Ref. [21] and to 0.35, 0.56, and 0.85 at $T = 0.82T_C$ for the bundle cell in Ref. [20]. The signal-to-noise ratios of the NMR spectra shown in Fig. 1 were improved compared with those in Ref. [21] and two peaks of the blue signal and three peaks of the red and green signal were clearly distinguished. The relative intensities of the peaks with small R_t^2 in a single cylinder are much larger than those in the bundle cell. The observation of several NMR peaks excludes some textures with only one peak from the six candidates mentioned above. The possible candidates are the three types of textures MH-ax, MH-hb, and RD-hb (see Fig. 3(b) in Ref. [21]). It is known that a spin wave with small R_t^2 is excited in a wide NMR potential. From the smallest value of R_t^2 of the three NMR spectra, the red spectra in Fig. 1 should correspond to the MH-hb texture because the MH-hb texture has a wider dipole-unlocked region than the other two textures (see below). We discuss each texture more precisely and compare the NMR spectra with the spin wave mode below.

We show the result of the analysis for the MH-ax texture in Fig. 2, for the RD-hb texture in Fig. 3, and for the MH-hb texture in Fig. 4 at $P = 3.3$ MPa, $T = 0.80T_C$, and $\Omega = 0$ rad/s. The procedure of the numerical calculation is as follows [17]. At first, assuming a possible candidate of the texture, the equilibrium texture is determined so as to minimize the free energy for a given ξ_D such as Fig. 2(a), Fig. 3(a), and Fig. 4(a), respectively. The light blue corresponds to the dipole-locked region. Next, we derive the resonance frequencies and wave functions of the spin waves excited in the NMR potential of the equilibrium texture. The wave function of the first spin wave mode excited in each texture is shown in Fig. 2(b), Fig. 3(b), and Fig. 4(b), respectively. Finally, we yield the relative intensity of each spin wave mode from the wave function assuming the uniform oscillating H_1 field in the NMR coil. As shown in Fig. 2(a), in the MH-ax texture, the **l**- and **d**-vectors are radially perpendicular to the cylindrical surface only near the edge; they deviate from this direction and are parallel to the cylindrical axis in the central region. The **l**- and **d**-vectors are parallel to each other at the edge (dipole locked), whereas near the center they are not parallel to each other (dipole unlocked) because the healing length of the **l**-vector is determined by the dipole coherence length $\xi_D \approx 10$ μm while the healing length of the **d**-vector is dominated by the magnetic healing length $\xi_H \approx 1$ μm. As shown in Fig. 3(a), in the RD-hb texture, where all the order parameter vectors are perpendicular to the cylindrical axis, the **l**-vectors point radially and the **d**-vectors point to the vertical direction and are bent slightly by the dipole interaction near the edge. At the thin edge regions of the top and bottom sides, the **l**- and **d**-vectors are parallel in a nearly dipole-locked state, while in other regions they are almost in an unlocked state. As shown in Fig. 4(a), in the MH-hb texture, the **d**-vectors point to the horizontal direction and are bent slightly by the dipole interaction near the edge which is similar to the distribution of the **d**-vectors in the RD-hb texture. The **l**-vectors are almost radially distributed in the same manner as for the MH-ax but the region of the red arrows are vertically distorted because of the dipole interaction. The dipole-locked region appears at the thin edge regions of the left and right sides, while the remaining area is unlocked and much larger than those in Figs. 2(a) and 3(a).

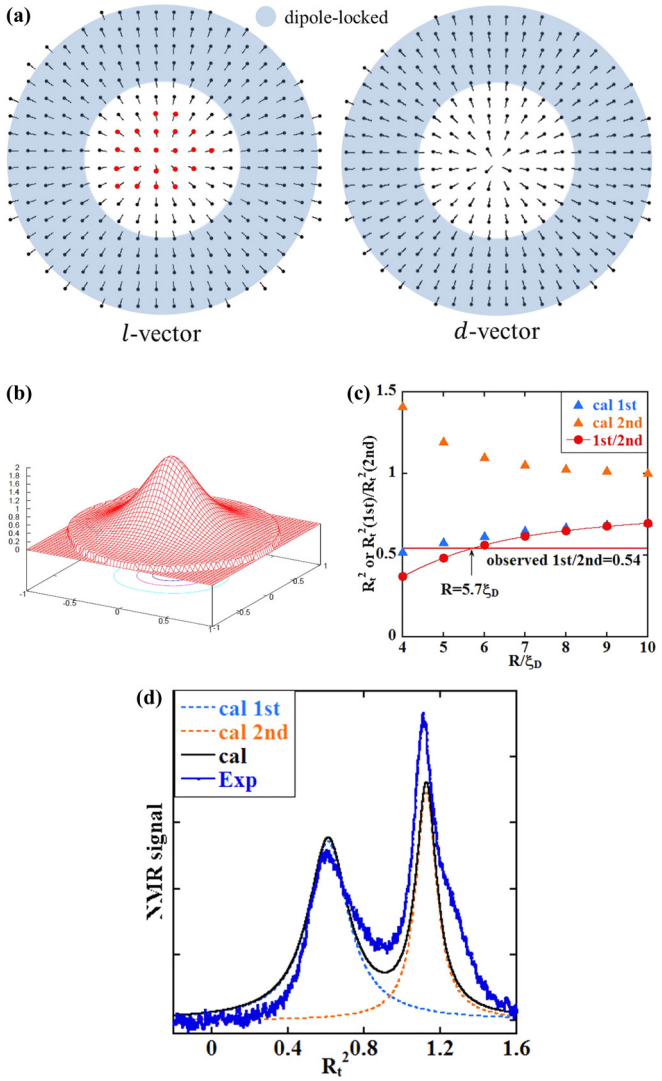

FIG. 2. (Color online) The result of the analysis for the MH-ax texture at 3.3 MPa, $T = 0.80T_C$, and $\Omega = 0$ rad/s. The numerical calculations in (a), (b), and (d) were performed with $R/\xi_D = 5.7$. (a) Cross-section view of calculated stable textures for the **l**- and **d**-vectors. The arrows indicate the component along the plane of paper and the red arrows show that they are inclined at the angle of more than 45° against the plane. (b) Calculated wave function of the first spin wave mode. The bottom view indicates the contour line. (c) Calculated R_t^2 of excited spin wave modes and the ratio of R_t^2 of the first mode (unlocked region) to that of the second mode (locked region) for various R/ξ_D. (d) Comparison between the calculated and observed spectra. The observed spectrum is the same as that in Fig. 1. The linewidth of each mode was adjusted so as to match the observed spectrum.

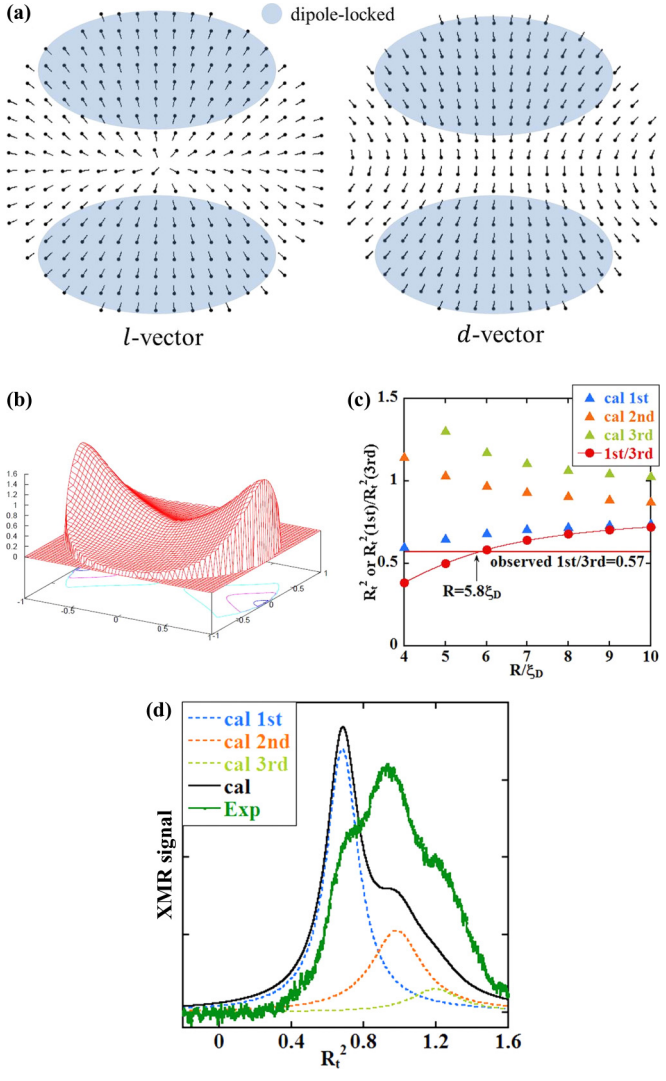

FIG. 3. (Color online) The result of the analysis for the RD-hb texture at 3.3 MPa, $T = 0.80T_C$, and $\Omega = 0$ rad/s. The numerical calculations in (a), (b), and (d) were performed with $R/\xi_D = 5.8$. (a) Cross-section view of calculated stable textures for the **l**- and **d**-vectors. The arrows indicate the component along the plane of paper. (b) Calculated wave function of the first spin wave mode. The bottom view indicates the contour line. (c) Calculated R_t^2 of excited spin wave modes and the ratio of R_t^2 of the first mode (unlocked region) to that of the third mode (locked region) for various R/ξ_D. (d) Comparison between the calculated and observed spectra. The observed spectrum is the same as that in Fig. 1. The linewidth of each mode was adjusted so as to match the observed spectrum.

From numerical calculations, it was found that only two spin wave modes are excited in the MH-ax texture while three spin wave modes are excited in the RD-hb and MH-hb textures. This strongly suggests that we should associate the blue spectrum with two peaks in Fig. 1 with the MH-ax texture. In the MH-ax texture, the first spin wave mode is excited near the center of the cylinder (unlocked region) and the second mode is excited near the edge (locked region). The wave function of the first spin wave mode excited in the MH-ax texture is shown in Fig. 2(b). The calculated R_t^2 of two spin wave modes for various R/ξ_D and the ratio of R_t^2 of the first mode (unlocked region) to R_t^2 of the second mode (locked region) are plotted in Fig. 2(c). On the other hand the MH-hb and RD-hb textures exhibit three spin wave modes. In a similar way as for the MH-ax texture, R_t^2 of the three spin wave modes for various R/ξ_D and the ratio of R_t^2 of the first mode (unlocked region) to R_t^2 of the third mode (locked region) are plotted in Fig. 3(c) and Fig. 4(c) for the RD-hb and MH-hb textures, respectively. It is also found by numerical calculation that the smallest R_t^2 of the first mode in the MH-hb texture is much

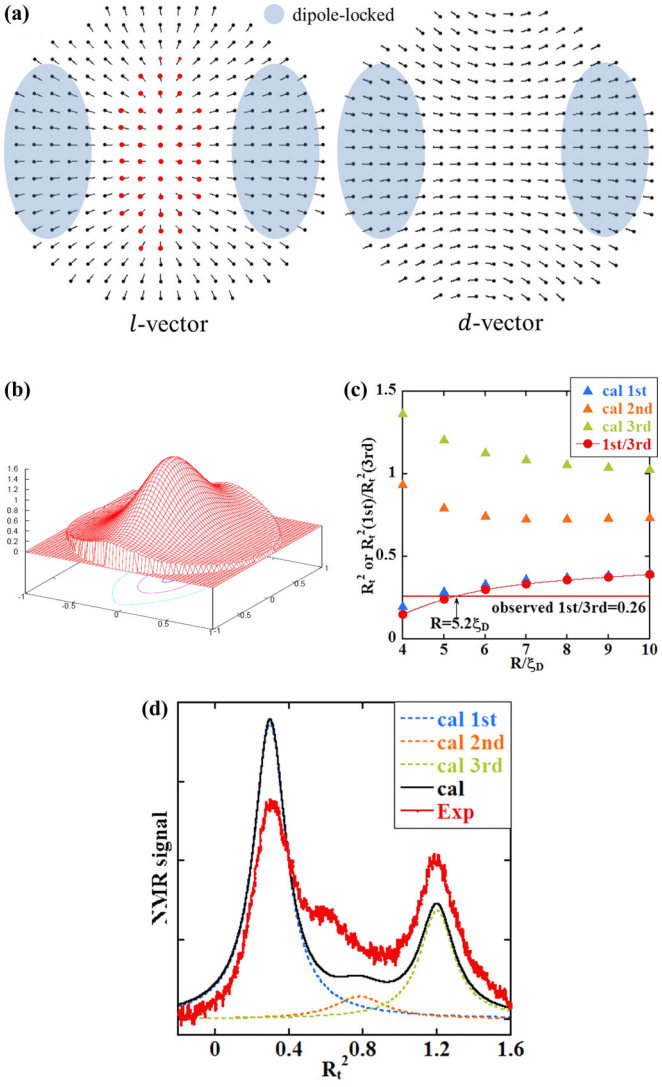

FIG. 4. (Color online) The result of the analysis for the MH-hb texture at 3.3 MPa, $T = 0.80T_C$, and $\Omega = 0$ rad/s. The numerical calculations in (a), (b), and (d) were performed with $R/\xi_D = 5.2$. (a) Cross-section view of calculated stable textures for the **l**- and **d**-vectors. The arrows indicate the component along the plane of paper and the red arrows show that they are inclined at the angle of more than 45° against the plane. (b) Calculated wave function of the first spin wave mode. The bottom view indicates the contour line. (c) Calculated R_t^2 of excited spin wave modes and the ratio of R_t^2 of the first mode (unlocked region) to that of the third mode (locked region) for various R/ξ_D. (d) Comparison between the calculated and observed spectra. The observed spectrum is the same as that in Fig. 1. The linewidth of each mode was adjusted so as to match the observed spectrum.

smaller than that in the RD-hb texture. Hence we associate the green spectrum in Fig. 1 with the RD-hb texture and the red spectrum with MH-hb. The experimentally obtained $R_t^2(1st)/R_t^2(2nd)$ for the blue spectrum is 0.54 ± 0.01 and $R_t^2(1st)/R_t^2(3rd)$ for the green and red spectra are 0.57 ± 0.01 and 0.26 ± 0.01, respectively. By comparing these values with the numerical results in Fig. 2(c), Fig. 3(c), and Fig. 4(c), we obtain $R/\xi_D = 5.7 \pm 0.1, 5.8 \pm 0.1$, and 5.2 ± 0.1 for the MH-ax, RD-hb, and MH-hb textures, respectively. The

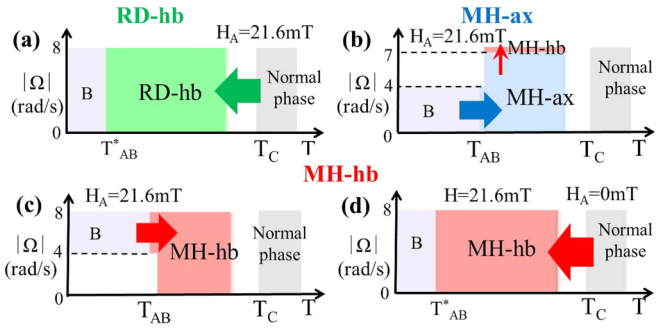

FIG. 5. (Color online) Phase diagrams of the three types of textures observed in a narrow cylinder at $H_A = 21.6f$ and 0 mT. H_A is the magnetic field applied when the liquid enters the A phase. (a) RD-hb texture, (b) MH-ax texture, and (c) MH-hb texture at $H_A = 21.6$ mT. (d) MH-hb texture at $H_A = 0$ mT. The NMR measurements are performed at $H = 21.6$ mT applied in the A phase. T_{AB} and T_{AB}^* are warmed and supercooled transition temperatures between the A phase and B phase, respectively.

obtained mean value of ξ_D is 9.0 μm, which is close to the estimated value of 10 μm.

We calculated the NMR spectra in the Lorentzian form for each spin wave using R_t^2 corresponding to the obtained R/ξ_D and also using the linewidth estimated to match the experimental NMR spectra. Each mode height was derived from the estimated linewidth and the relative intensity given by numerical calculation of the spin wave mode. The calculated spectra are plotted in Fig. 2(d), Fig. 3(d), and Fig. 4(d) denoted by "cal 1st" "cal 2nd" and "cal 3rd" for the first, second, and third spin wave modes and by "cal" for their sum, and the observed spectra are shown by "Exp". The calculated spectra of the MH-ax and MH-hb textures explain the observed blue and red spectra very well, respectively. However, we can see discrepancies in the relative intensities in Fig. 3(d) between the spectra of the RD-hb texture and the green spectra, though the resonance frequencies agree quite well with each other. The reason for this discrepancy is not clear.

Based on all the above, we conclude that the red, blue, and green spectra in Fig. 1 are due to spin wave modes in the MH-hb, MH-ax, and RD-hb textures, respectively. That the resonance frequency of each NMR peak matches the numerically calculated one of the spin wave mode ensures that a unique texture is nucleated in the cylinder cell.

The phase diagrams of the three types of textures are given in Fig. 5 at $H_A = 21.6$ mT and 0 mT, where H_A means the applied magnetic field when the liquid enters the A phase. We cannot distinguish the various textures near T_C because of small frequency shifts of the spin waves due to the small Leggett frequency. The phase diagrams do not depend on the direction of rotation. We always get exactly the same spectra each time we perform a measurement. In $H_A = 21.6$ mT, the RD-hb texture is always obtained when the liquid is cooled from the normal phase to the A phase under a constant rotation Ω, as shown in Fig. 5(a). This Rd-hb texture is stable for varying temperatures and rotation angular velocities. On the other hand, when the liquid enters the A phase from the B phase by warming, the MH-ax texture is obtained for the case of $\Omega < 4$ rad/s as shown in Fig. 5(b). However, for the case

of $\Omega > 4$ rad/s, the MH-hb texture is obtained as shown in Fig. 5(c). The obtained MH-ax texture is converted to the MH-hb texture by increasing Ω at a constant temperature as shown in Fig. 5(b). The critical Ω for the textural transition ranges between 7 and 8 rad/s. Once the MH-hb texture is formed from the MH-ax texture, this MH-hb texture is very stable even for changing temperature and Ω and shows the same stable region as in Fig. 5(c). We think that these hysteretic behaviors can be attributed to the fact that the textural transition is a first-order transition. On the other hand, no textural transition from the MH-ax texture is observed by varying temperatures below T_C and Ω below the critical Ω, as shown in Fig. 5(b).

According to the numerical calculation under a magnetic field (see Fig. 11 in Ref. [13]), the RD-hb texture becomes stable near T_C and the MH-hb texture becomes stable under a large rotation angular velocity far below T_C. The observed textures in the A phase shown in Figs. 5(a) and 5(c) are consistent with Ref. [13]. However, the textural transitions between the RD-hb and MH-hb textures by changing temperatures and Ω expected in Ref. [13] are not observed. We think this is because the transition is a first-order transition and also involves the nucleation and annihilation of singularity. On the other hand, unlike the numerical calculation, the MH-ax texture is formed by the transition from the B phase to A phase at small rotation angular velocity less than 4 rad/s. In the B phase, we do not observe the transformation of the NMR spectra due to the penetration of the vortex by changing the rotation angular velocity such as the spin wave or the shift of the NMR spectrum to higher resonance frequency [22]. This is because the critical angular velocity of the vortex penetration in the B phase cannot be exceeded in our experimental setup, which is about 70 rad/s estimated from the observed value of 4.5 rad/s in the A phase confined into the cylinder volume with a radius of 115 μm [9]. Our observation of the MH-ax and MH-hb textures by the transition from the B phase to A phase supports that any singularities in the A phase are not formed when the interface between the A phase and vortex-free B phase moves through the cylinder volume. As shown in Fig. 6 of Ref. [13], the **l**-vectors of the MH-ax texture distribute axisymmetrically and gradually rise along the cylinder axis with the length scale of ξ_D. Therefore the large mass current emerges at a distance of ξ_D from the center (Fig. 6(d) of Ref. [13]). On the other hand, as shown in Fig. 4 of Ref. [13], the **l**-vectors of the MH-hb texture orient as the same as those of the MH-ax texture along the horizontal direction but, along the vertical direction, rise along the cylinder axis with larger length scale of R because **l**- and **d**-vectors are dipole-unlocked from each other in that region. Therefore the large mass current flows near the edge along the vertical direction (y axis in Fig. 4(d) in Ref. [13]). In consequence the MH-hb texture is more favorable to be formed than the MH-ax texture at larger Ω because of the larger angular momentum due to the mass current at the edge.

When the liquid is cooled from the normal phase to the A phase at $H_A = 0$ and 0.5 mT, the MH-hb texture is obtained by NMR after applying a magnetic field of $H = 21.6$ mT, as shown in Fig. 5(d). The RD-hb texture, however, is observed at $H_A = 1$ mT. The numerical calculation shows that the MH-ax texture is stable in low magnetic field (see Fig. 10 in Ref. [13]). However, applying the magnetic field for NMR might have changed the distribution of the **d**-vectors from ax type to hb type because of the anisotropic magnetic energy. Thus the observed MH-hb texture may not necessarily contradict the result shown in Ref. [13].

We investigated three types of textures of superfluid ^{3}He-A phase observed in a single narrow cylinder. The calculated spin waves in the three textures, MH-ax, RD-hb, and MH-hb, explain the three observed NMR spectra very well. What kind of texture appears depends on the experimental conditions at the onset of the A phase. The obtained phase diagram of texture is partly consistent with the theoretical treatment. The controlled generation of the MH-hb texture allows us to investigate the paradox of the orbital angular momentum because the **l**-vectors of the MH texture align along the cylinder axis in its core region [17] and the MH-hb texture is very stable with respect to Ω.

The authors would like to thank Prof. T. Mizusaki for his contributions in the earlier stage of this research program. This work was supported by Grant-in Aid for Scientific Research on Innovative Areas "Topological Quantum Phenomena" (Grant No. 22103003) and Grant-in-Aid for Scientific Research on Priority Area "Physics of New Quantum Phases in Superclean Materials" (Grant No. 17071009) from the Ministry of Education, Culture, Sports, Science and Technology (MEXT) of Japan. This work was carried out under the Visiting Researcher's Program of the Institute for Solid State Physics, the University of Tokyo.

[1] D. Vollhardt and P. Wölfle, *The Superfluid Phases of Helium 3* (Taylor & Francis, New York, 1990).
[2] Y. Tsutsumi and K. Machida, Phys. Rev. A **80**, 035601 (2009).
[3] T. H. R. Skyrme, Proc. R. Soc. A **260**, 127 (1961).
[4] A. Vilenkin, Phys. Rev. D **23**, 852 (1981).
[5] M. Yamashita, K. Izumina, A. Matsubara, Y. Sasaki, O. Ishikawa, T. Takagi, M. Kubota, and T. Mizusaki, Phys. Rev. Lett. **101**, 025302 (2008).
[6] P. M. Walmsley, D. J. Cousins, and A. I. Golov, Phys. Rev. Lett. **91**, 225301 (2003).
[7] R. Ishiguro, O. Ishikawa, M. Yamashita, Y. Sasaki, K. Fukuda, M. Kubota, H. Ishimoto, R. E. Packard, T. Takagi, T. Ohmi, and T. Mizusaki, Phys. Rev. Lett. **93**, 125301 (2004).
[8] V. M. H. Ruutu, J. Kopu, M. Krusius, Ü. Parts, B. Placais, E. V. Thuneberg, and W. Xu, Phys. Rev. Lett. **79**, 5058 (1997).
[9] R. Ishiguro, O. Ishikawa, M. Yamashita, Y. Sasaki, K. Fukuda, M. Kubota, H. Ishimoto, R. E. Packard, T. Takagi, T. Ohmi, and T. Mizusaki, J. Phys.: Conf. Ser. **150**, 032033 (2009).
[10] P. G. de Gennes, Phys. Lett. A **44**, 271 (1973).
[11] K. Maki, J. Low Temp. Phys. **32**, 1 (1978).
[12] N. D. Mermin and T.-L. Ho, Phys. Rev. Lett **36**, 594 (1976).
[13] Y. Tsutsumi and K. Machida, J. Phys. Soc. Jpn. **78**, 114606 (2009).
[14] T. Kita, J. Phys. Soc. Jpn. **67**, 216 (1998).
[15] J. A. Sauls, Phys. Lett. B **84**, 214509 (2011).
[16] F. Gaitan, Phys. Lett. A **178**, 419 (1993).

[17] T. Takagi, J. Phys. Soc. Jpn. **65**, 1722 (1996).
[18] M. C. Cross, J. Low Temp. Phys. **26**, 165 (1977).
[19] M. Kubota, T. Obata, R. Ishiguro, M. Yamashita, T. Igarashi, E. Hayata, O. Ishikawa, Y. Sasaki, N. Mikhin, M. Fukuda, V. Kovacik, and T. Mizusaki, Physica B **329–333**, 1577 (2003).
[20] R. Ishiguro, Ph.D. thesis, Kyoto University, 2003.
[21] T. Kunimatsu, H. Nema, R. Ishiguro, M. Kubota, T. Takagi, Y. Sasaki, and O. Ishikawa, J. Low Temp. Phys. **171**, 280 (2013).
[22] P. J. Hakonen, M. Krusius, M. M. Salomaa, R. H. Salmelin, and J. T. Simola, J. Low Temp. Phys. **76**, 225 (1989).